

## Designing a New Scrap-Based Continuous Steelmaking Process using CFD Simulation

Lifeng Zhang

Jun Aoki

Brian G. Thomas

Dept. of Mechanical & Industrial Engineering

University of Illinois at Urbana-Champaign

1206 W. Green St., Urbana, IL 61801, U.S.A

Email: zhang25@uiuc.edu, bgthomas@uiuc.edu

Tel: 1-217-244-4656, Fax: 1-217-244-6534

Jörg Peter

Kent D. Peaslee

Department of Material Science and Engineering

University of Missouri-Rolla

218 McNutt Hall, 1870 Miner Circle, Rolla, MO 65409-0340

Email: kpeaslee@umr.edu,

Tel: 573-341-4714, Fax: 573-341-6934

Key words: Continuous Steelmaking Process, Multiphase Fluid Flow, Bubbles, Inclusions, Mixing

### INTRODUCTION

Computational fluid dynamics (CFD) models of turbulent, multiphase flow are applied to help develop a new scrap-based process for continuous steelmaking, which aims to revolutionize the way that steel is made in the 21<sup>st</sup> century. Steel has always been made by batch processing which involves high labor requirements, energy losses, yield losses, environmental problems, inconsistent quality between heats, automation difficulties, and is limited to specific heat sizes. Continuous steelmaking has the potential to use energy more efficiently, lower production costs, lessen environmental impact, and increase steel quality and consistency. Many different continuous steelmaking processes have been proposed in the last 40 years.<sup>[1, 2]</sup> Some of these processes even reached the pilot-plant stage, but none has yet been fully commercialized. A schematic of the current proposed process is shown in **Figure 1**. Steel continuously flows through five interconnected vessels during this continuous steelmaking process. Preheated scrap is continuously charged and melted in the first vessel (modified AC Consteel EAF). Decarburization and dephosphorising are achieved in the second vessel (Oxidizer), if needed. In the third vessel (Reducer), steel is continuously deoxidized, desulfurized, and alloyed. Steel with a near-final composition enters the fourth vessel (Finisher) for final alloy trimming, additional desulfurization, inclusion floatation, thermal and chemical homogenization, before flowing into the fifth vessel (Tundish). Further details are given in another paper.<sup>[3]</sup> This new design is based on analysis of previous literature, discussions between the researchers in this project, numerical simulations<sup>[4, 5]</sup>, and water models<sup>[6]</sup>. The purpose of this paper is to introduce the powerful tool of CFD in designing metallurgical processes in general, and this new continuous steelmaking process in particular.

Owing to the tremendous cost of pilot-plant-scale industrial trials, previous attempts to develop new metallurgical processes have generally relied on scaling up small bench-scale experiments. Due to the lack of true understanding of the rate constants, mixing phenomena, and geometric effects which control the success of the real process, many previous pilot-plant operations have been unsuccessful. With the tremendous increases in the power of computer hardware and modeling software, computational modeling offers a better design tool for creating new processes. Numerical simulation has the potential to quantify the phenomena taking place in a commercial-scale process before it is constructed. In order to achieve success, the model must accurately predict the phenomena of true interest, which for steelmaking processes include:

- Multiphase and turbulent fluid flow and within each vessel in the process, incorporating the effects of gas stirring (oxygen gas or argon gas), and including transient variations, which are the main source of variability in the product

- Mixing phenomena in each vessel, including solidification, heating, and remelting of a steel layer around alloy particle additions, which directly controls the success of alloying, and is important to other reactions as well
- Inclusion nucleation, growth, motion and removal in the molten steel;
- Heat transfer phenomena, including temperature drops between each vessel;
- Evolution of composition during each vessel, including the thermodynamics and kinetics of the reactions between the molten steel and interfaces with the top slag and bubble surfaces, coupled with fluid flow and mixing phenomena;
- Effects of the true three-dimensional features of the vessel shape (including location of inlet and outlet launder), gas injection location and flow rates, and other operating conditions on the above phenomena.

These phenomena are equally important to conventional steelmaking processes. Thus, initial development of the computational models has focused on model validation by matching with industrial measurements of fluid flow and alloy dispersion in the molten steel during LMF steel refining. [7, 8] Although much work remains to be done regarding model development, the current paper is to show how the modeling tools have already been applied to help design the new process. Specifically, this paper presents numerical simulations to compare two different designs of the oxidizer vessel, based on the fluid flow, mixing phenomena and inclusion motion. The second design was chosen to improve on perceived faults in the first design, including impingement of the inlet jet on the bottom of the inlet launder, and short circuiting of the fluid flow pattern. Further examples of vessel designs based on numerical simulations are planned for future publications.

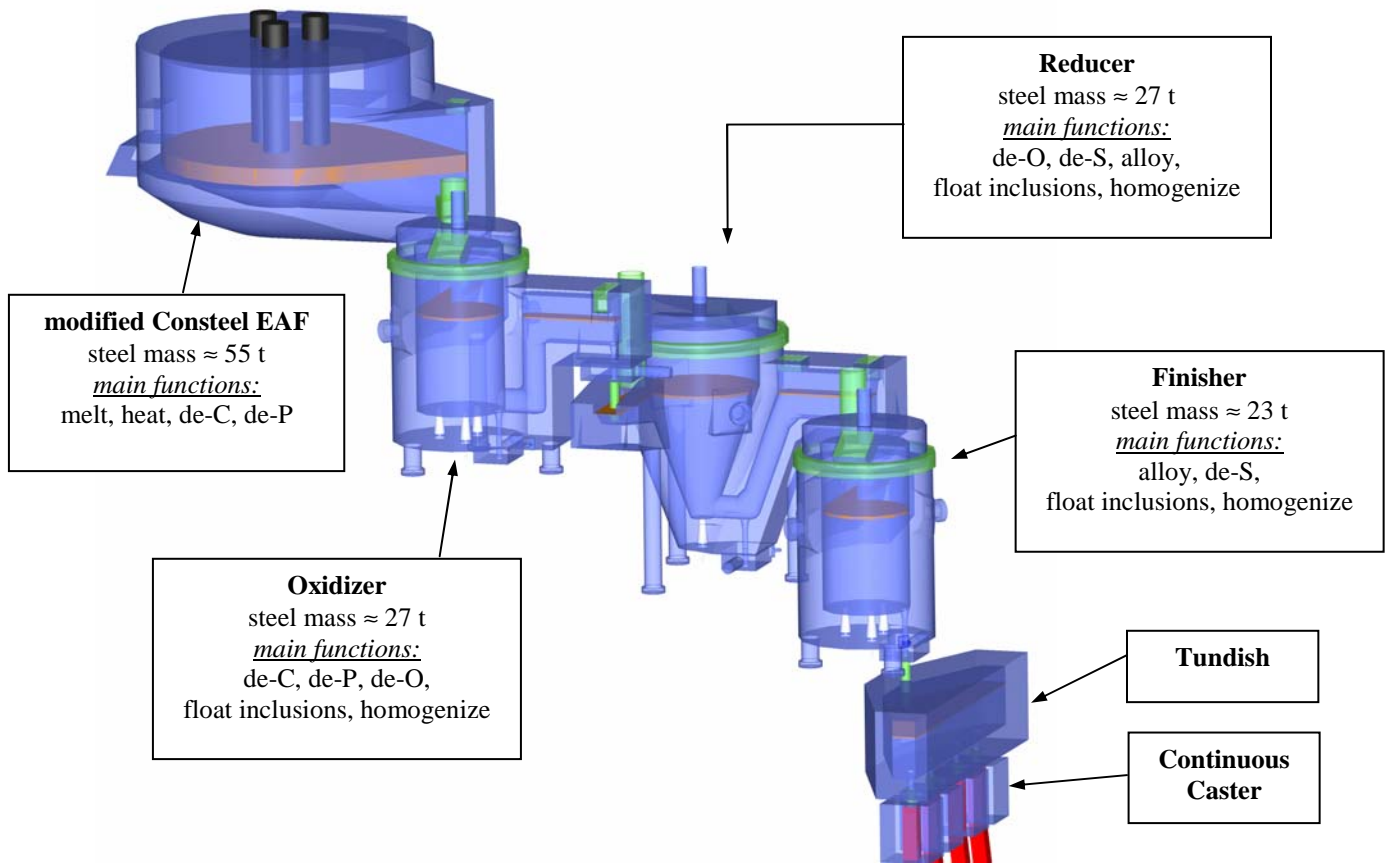


Fig.1 Transparent side view of the fully continuous steelmaking process

## MATHEMATICAL FORMULATIONS AND COMPUTATION CONDITIONS

### Single Phase Fluid Flow

The equations for transient three-dimensional fluid flow are solved in this work. The  $k-\epsilon$  two-equation model is used to simulate turbulence, which solves two equations for the transport of turbulent kinetic energy and its dissipation rate to obtain the effective viscosity field,  $\mu_{\text{eff}}$ . [9, 10]

### Particle Motion

The trajectory of each particle (bubble and inclusion) is calculated by integrating its local velocity, defined by considering the different forces which act on it, as given in Eq.(1) for direction  $i$ .

$$\frac{du_{pi}}{dt} = F_D(u_i - u_{pi}) + \frac{\rho_p - \rho}{\rho} g_i + \frac{1}{2} \frac{\rho}{\rho_p} \frac{d}{dt} (u_i - u_{pi}) + \frac{\rho}{\rho_p} u_i \frac{\partial u_i}{\partial x_i}, \quad (1)$$

$$F_D = \frac{18\mu}{\rho_p d_p^2} \frac{C_D \text{Re}_p}{24} \quad (2)$$

$$\text{Re}_p = \frac{\rho d_p |u - u_p|}{\mu} \quad (3)$$

$$C_D = \frac{24}{\text{Re}_p} (1 + 0.186 \text{Re}_p^{0.6529}) \quad (4)$$

where  $\rho_p$  and  $\rho$  are the particle and liquid densities ( $\text{kg/m}^3$ ),  $u_i$  and  $u_{pi}$  are fluid velocity and particle velocity at direction  $i$  (m/s),  $t$  is time (s),  $C_D$  is the drag coefficient<sup>[11]</sup> as a function of particle Reynolds number ( $\text{Re}_p$ ),  $g$  is gravity acceleration,  $\mu$  viscosity of the fluid ( $\text{kg/m-s}$ ), and  $d_p$  is particle diameter (m).

The first term in Eq.(1) is the drag force per unit particle mass. The second term is the gravitational force, the third term is the “virtual mass” force<sup>[12]</sup> accelerating the fluid surrounding the particle, and the fourth term is the force stemming from the pressure gradient in the fluid.

The effect of turbulent fluctuation on particle motion can be modeled crudely by adding a random velocity fluctuation ( $\xi\sqrt{2k/3}$ ) to the mean fluid phase velocity at each step, where  $\xi$  is a random number and  $k$  is the local turbulent kinetic energy, i.e.,

$$u = \bar{u} + \xi\sqrt{2k/3} \quad (5)$$

## Multiphase Fluid Flow

Lagrangian Multi-Phase Model<sup>[13]</sup> is used to simulate the argon gas stirred multiphase fluid flow in this work. In this model, only one velocity field is solved (the Eulerian fluid phase), but the liquid volume fraction is included in every term. The liquid volume fraction is calculated from the gas volume fraction, which is solved from the particle trajectory calculations Eq. (1). As the trajectory of a bubble is computed, the momentum gained or lost by the bubble motion is incorporated in the subsequent continuous phase calculations. Two-way coupling is accomplished by alternately solving the discrete and continuous phase equations until the solutions in both phases have stopped changing. The momentum transfer from the continuous phase to the discrete phase is computed by examining the change in momentum of each bubble as it passes through each control volume. This momentum exchange is given by Eq.(6), which appears as a sink term in the continuous phase momentum balance equations.

$$F_i = \sum_{cell} \left\{ \left[ F_D(u_i - u_{pi}) + \frac{\rho_p - \rho}{\rho} g_i + \frac{1}{2} \frac{\rho}{\rho_p} \frac{d}{dt} (u_i - u_{pi}) + \frac{\rho}{\rho_p} u_i \frac{\partial u_i}{\partial x} \right] \cdot m_p \cdot \Delta t \right\}, \quad (6)$$

where the sum is over all the bubbles in the cell,  $m_p$  is the mass flow rate of each bubble stream ( $\text{kg/s}$ ), and  $\Delta t$  is the time step (s).

## Solute Transport

Alloy dispersion or tracer dispersion were simulated by solving the following solute transport equation,

$$\frac{\partial C}{\partial t} + u_{ip} \frac{\partial C}{\partial x_i} = \frac{\partial}{\partial x_i} \left( D_{eff} \frac{\partial C}{\partial x_i} \right) \quad (7)$$

where  $C$  is the solute concentration or volume fraction,  $D_{eff}$  is the effective diffusion coefficient ( $\text{m}^2/\text{s}$ ), depending on turbulent viscosity, given by

$$D_{eff} = D_o + \frac{\mu_{eff}}{\rho \cdot \text{Sc}_i} \quad (8)$$

where  $D_o$  is the laminar diffusion coefficient ( $\text{m}^2/\text{s}$ ),  $\mu_{eff}$  is the effective turbulent viscosity ( $\text{kg/m-s}$ ), and  $\text{Sc}_i$  is the turbulent Schmidt number, set here to equal 0.7.

## Boundary Conditions

For the simulation of fluid flow, a fixed velocity condition is imposed at the domain inlet, and a “pressure outlet condition” is used at the outlets. The top surface is assumed to be flat and no slag phase, with zero shear stress. No-slip boundary condition is used at wall, with standard “wall functions” in order to capture the steep gradients with reasonable accuracy on a coarse grid.<sup>[10, 14, 15]</sup> The particles are assumed to escape at the top surface and the outlet, and be reflected at other walls. 5000-10000 inclusions each size are injected into the domain through the inlet in order to get a statistical average of inclusion removal to the top surface. For the solute transport,

the zero flux boundary condition is used at walls and top surface, and zero concentration at outlet. All of the equations are solved using FLUENT [16].

### Computation Parameters

The vessel is cylindrical, with an inlet launder and an outlet launder, as shown in **Figure 2**. In Design I, gas is injected from the two porous plugs at the bottom, and in Design II there are three porous plugs at the bottom. The parameters are shown in **Table 1**. In Table 1, the theoretical residence time of the molten steel is the ratio between the domain volume and the steel flow rate.

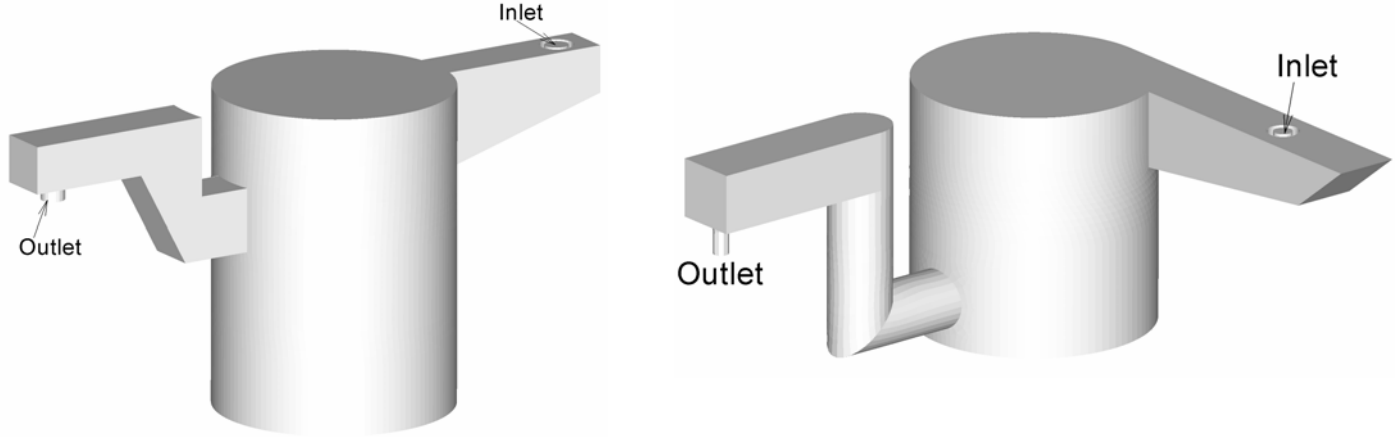


Fig.2 Schematic of Design I (left) and Design II (right) of the Oxidizer vessel in Fig.1

Table 1 Dimensions and parameters for the two designs of the Oxidizer Vessel

	Design I	Design II
Dimension of the vessel	φ1.4m, H2.0m	φ1.5m, H1.65m
Inside volume of the whole domain (m <sup>3</sup> )	3.393	3.636
Inner diameter of inlet (mm)	140	120
Submergence depth of the inlet shroud (mm)	220	150
Temperature of the molten steel (K)	1900	1900
Steel flow rate (tons/hour)	99.5	99.5
Steel flow rate (m <sup>3</sup> /s)	0.003572	0.003572
Theoretical residence time of the molten steel (s)	950	1018
Inlet velocity (m/s)	0.232	0.3158
Inlet turbulent energy (m <sup>2</sup> /s <sup>2</sup> )	3.1×10 <sup>-4</sup>	5.619×10 <sup>-4</sup>
Inlet turbulent energy dissipation rate (m <sup>2</sup> /s <sup>3</sup> )	4.0×10 <sup>-4</sup>	1.140×10 <sup>-3</sup>
Steel density (kg/m <sup>3</sup> )	7020	7020
Argon density (kg/m <sup>3</sup> )	1.6228	1.6228
Argon gas flow rate at 300K (m <sup>3</sup> /min)	0.49	0.49
Argon gas flow rate at 300K (m <sup>3</sup> /s)	0.01325	0.01325
Argon gas flow rate at 1900K (m <sup>3</sup> /s)	0.0219	0.0219
Bubble size at 1900K (mm)	36.4	31.0
Number of porous plug at the bottom	2	3
Total bubble injection at 1900K (#/s)	864	1406
Inclusion density (kg/m <sup>3</sup> )	5000	5000

The cold gas flow rate (at 300K)  $Q_{g,cold}$  can be converted to hot gas flow rate (at 1900K)  $Q_{g,hot}$  by Eq.(9).

$$Q_{g,hot} = Q_{g,cold} \frac{T_o P_\infty}{T_\infty (P_\infty + \rho g H)} \quad (9)$$

where  $P_\infty$  is room pressure.  $T_\infty=300K$ .  $T_o$  is the temperature of the molten steel, 1900K.  $H$  is the depth of molten steel in the vessel (m).

The bubble diameter  $d_B$  (m) depends on the gas flow rate according to: [17]

$$d_B = 0.35 \left( \frac{Q_g^2}{g} \right)^{0.2} \quad (10)$$

Thus the number of bubbles injected into the system per unit time  $N_B$  (#bubbles/s) can be expressed by

$$N_{B,hot} = \frac{Q_{gas,hot}}{V_{B,hot}} \quad (11)$$

where  $V_B$  is the volume of a single bubble

### FLUID FLOW AND PARTICLE MOTION WITHOUT ARGON INJECTION

Steady-state flow without gas injection in the vessel is calculated first. In Design I, a simple open-bottom inlet nozzle is used. As shown in **Figure 3**, the inlet jet from this nozzle design impinges strongly against the shallow bottom of the inlet launder, so splashing and erosion of the refractory bricks might be a problem. To avoid this problem, Design II uses a side-opened inlet nozzle, (like a one-port continuous casting nozzle), so there is minimal jet impingement on the bottom of the inlet launder. Without gas injection, in Design I, the molten steel enters the vessel from the inlet launder with a downward angle, quickly traverses across the vessel, then directly leaves through the outlet launder (**Figure 4**). This indicates strong short circuiting, which would be very detrimental for the process. Any time the gas injection failed, this situation would occur. To avoid this problem, Design II introduces a swirl into the flow by angling the inlet launder to avoid direct alignment with the outlet launder. As shown in Fig.3, a large, general swirl (rotating) flow pattern is generated in the whole domain. It should be noticed that without gas injection, in Design II, there is a strong backward flow toward the inlet launder along the top surface, which likely would push some slag along the surface towards the inlet nozzle (Fig4.b). In Design I, this back flow is not so strong when there is no gas injection. Fig.4b also indicates that Design II has less surface turbulence in the small space to the right hand of the nozzle when there is no gas injection. The surface velocity in the inlet launder of Design I is  $\leq 0.1\text{m/s}$ , and  $\leq 0.2\text{m/s}$  in Design II.

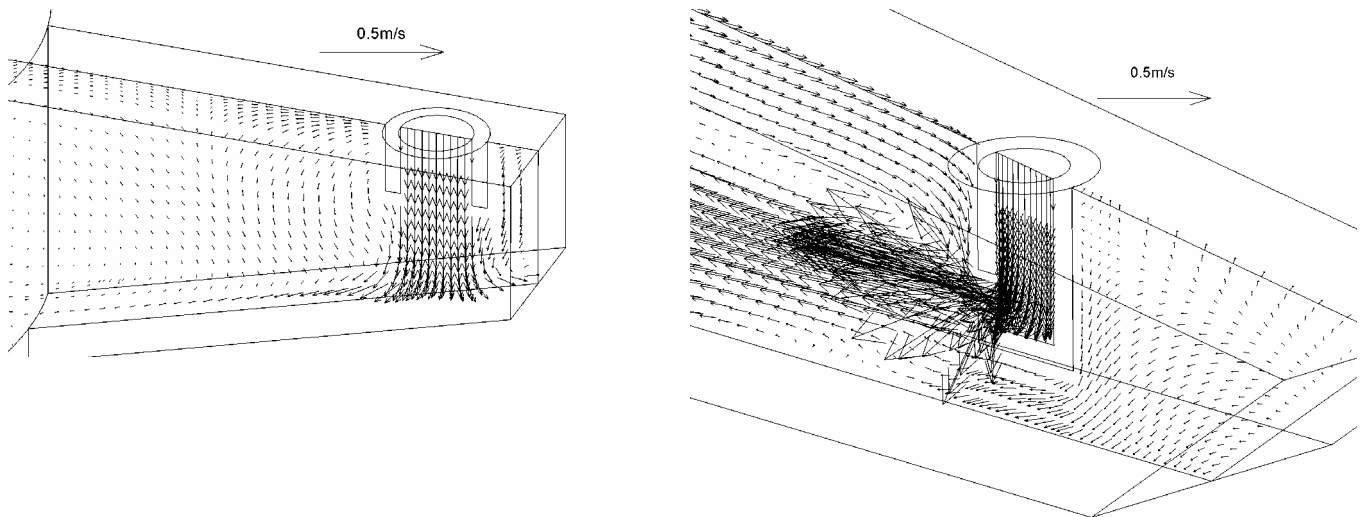
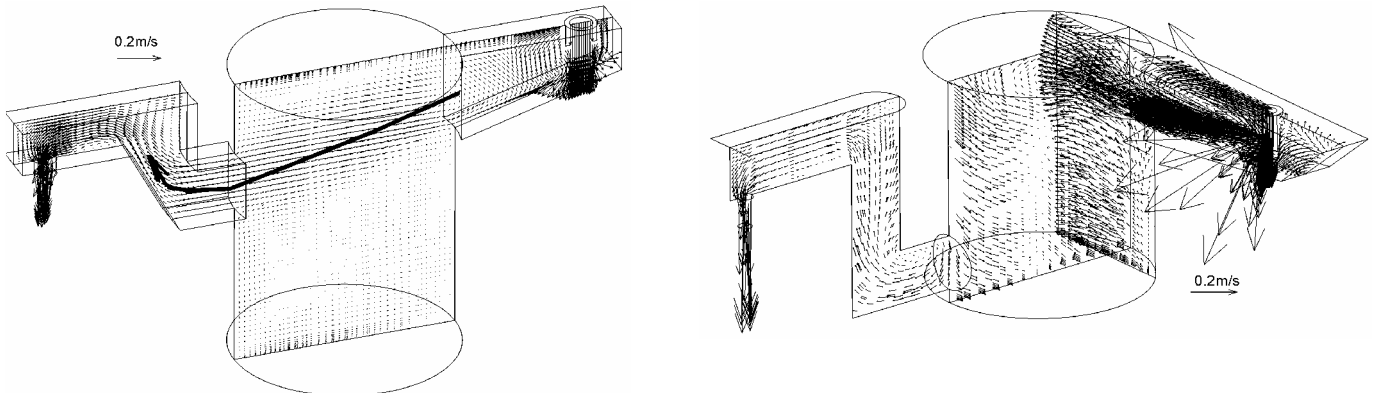
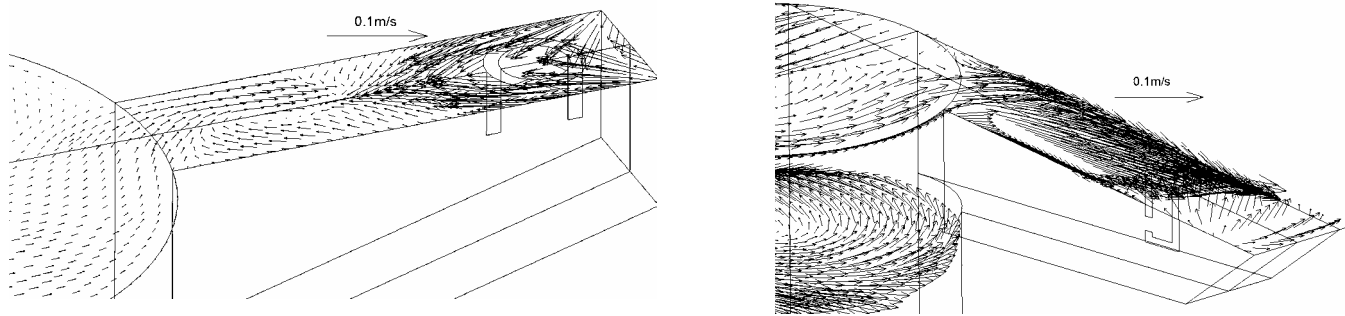


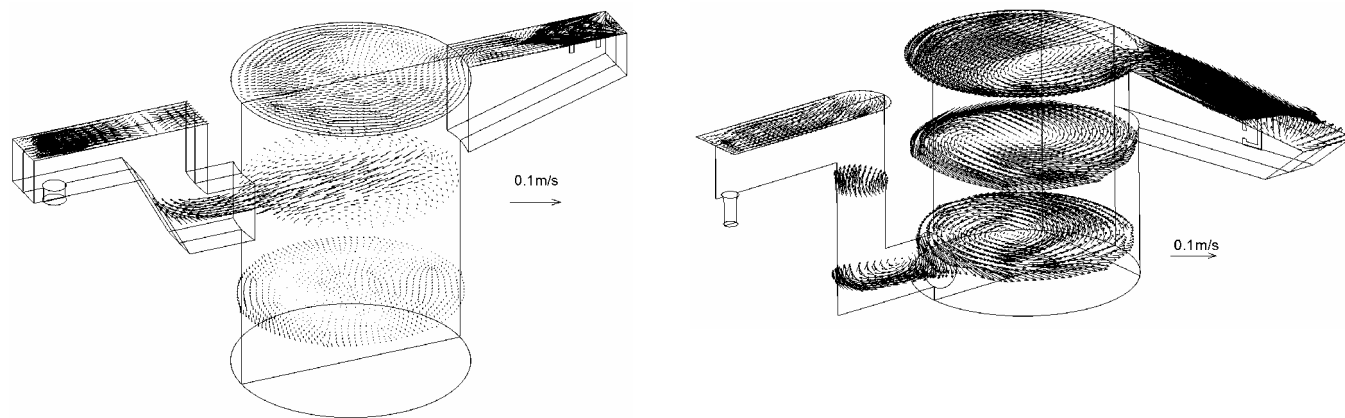
Fig.3 Velocities on centerline slices through the inlet launders in Design I (left) and II (right)



(a) Velocity within the centerline slice in Design I (left), and through inlet and outlet launders in Design II (right)



(b) Fluid flow velocities on the top surface of the inlet launder



(c) Fluid flow velocities in different horizontal sections in Design I (left) and II (right)

Fig.4 Fluid flow without gas injection in Design I (left) and Design II (right)

### FLUID FLOW AND PARTICLE MOTION WITH ARGON INJECTION

#### Fluid Flow

Argon gas is injected through the porous plugs at the bottom of each vessel. The argon gas flow rate is  $0.49 \text{ sm}^3/\text{min}$  (“cold” gas at  $25 \text{ }^\circ\text{C}$  and  $1\text{atm}$ ), and the bubble size is  $36.4\text{mm}$  for Design I, and  $31.0\text{mm}$  for Design II at  $1900\text{K}$ . **Figure 5** gives the iso-surface of  $0.001$  volume fraction of argon gas in the vessel. Design I seems to generate more dispersion of argon bubbles. The average residence time of bubbles in the vessel is  $1.24\text{s}$  in Design I, with an average rising speed of  $1.61\text{m/s}$ , while bubbles in Design II have an average residence time of  $0.87\text{s}$ , and rising speed of  $1.90\text{m/s}$ . The volume-averaged turbulent kinetic energy is  $2.76 \times 10^{-2} \text{ m}^2/\text{s}^2$  in Design I, and  $1.31 \times 10^{-2} \text{ m}^2/\text{s}^2$  in Design II. The volume-averaged turbulent energy dissipation rate is  $5.46 \times 10^{-2} \text{ m}^2/\text{s}^3$  in Design I, and  $2.15 \times 10^{-2} \text{ m}^2/\text{s}^3$  in Design II. At pseudo-steady state, there are 1075 bubbles in the entire liquid volume in Design I, and 1223 bubbles in Design II. The fluid flow velocities are shown in **Figure 6**, which indicates that Design II has a smaller average velocity than Design I. The volume-averaged velocity magnitude is  $0.241\text{m/s}$  in Design I, and is  $0.171\text{m/s}$  in Design II.

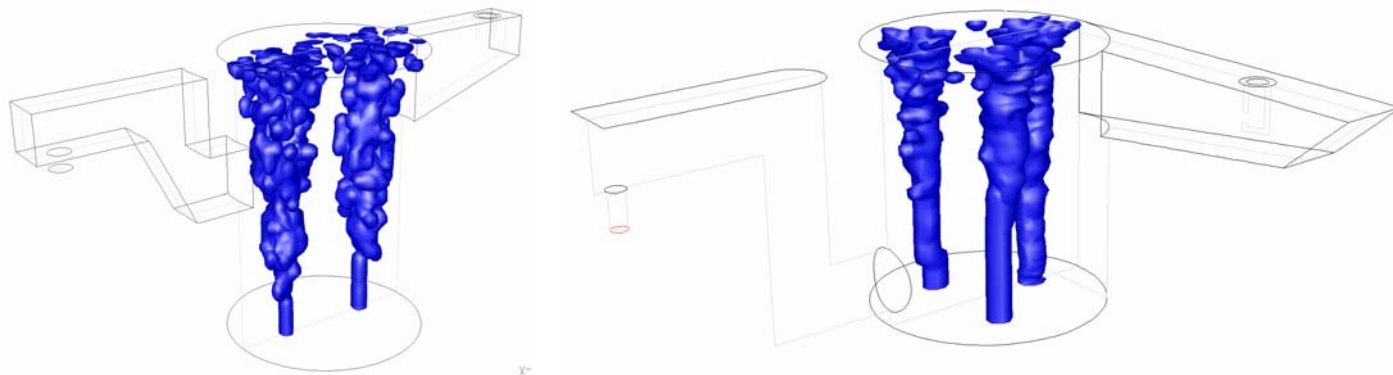


Fig.5 Bubble plumes in the vessel (Left: Design I, Right: Design II)

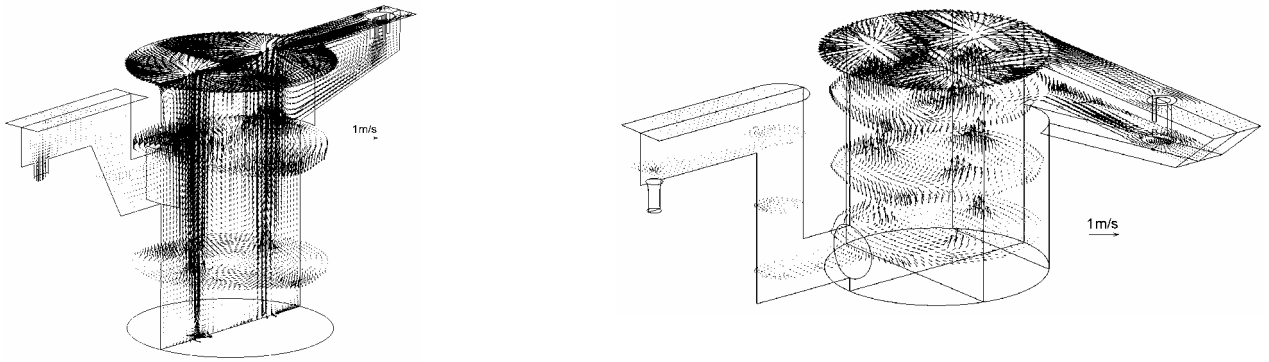
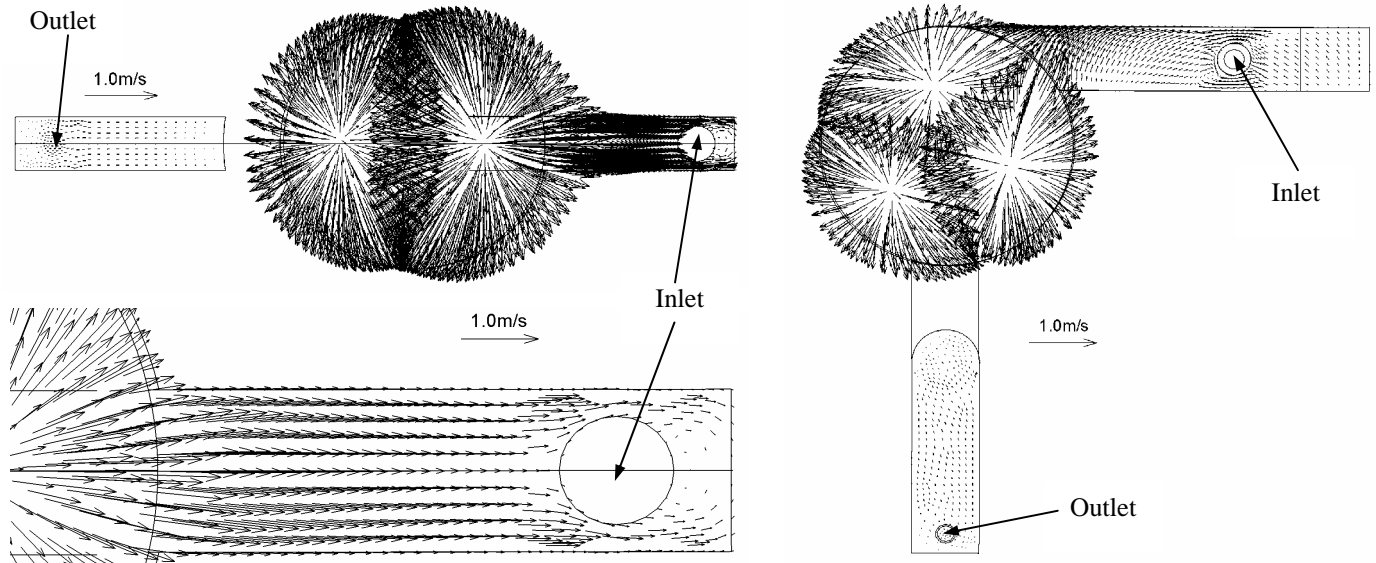
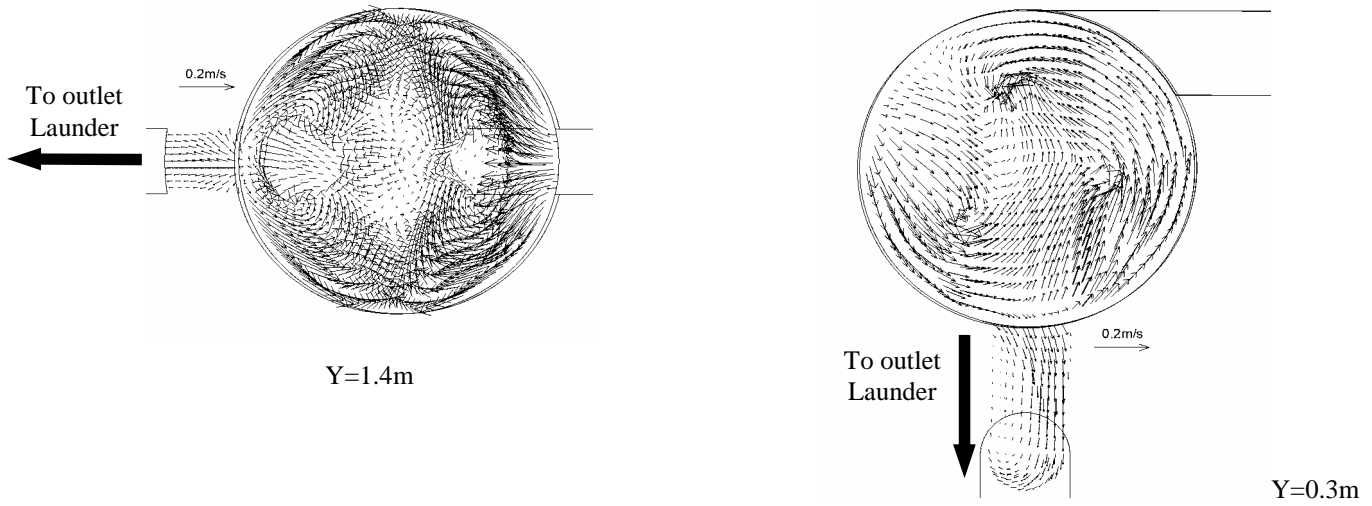


Fig.6 Fluid flow in the vessel (Left: Design I, Right: Design II)

Velocity distributions within some horizontal sections in the vessel are shown in **Figure 7**. With gas injection, the top surface has large velocities. There is a strong backflow along the top surface into the inlet launder in Design I. There is an asymmetrical (swirl) backflow along the top of the inlet launder in Design II, that is weaker than in Design I. The molten steel directly flows into the outlet launder from the main vessel in Design I (Fig.7a). In Design II, there is a strong swirl between the vessel and the outlet launder, as the rotating flow pattern in the vessel persists even though it is diminished somewhat by the three gas plumes (Fig.7b). Design I has two independent fully-recirculating flow patterns induced by the two gas plumes.



(a) At the top surface



(b) On the horizontal section passing through connection between the main vessel and the outlet launder

Fig.7 Velocity distribution details in two horizontal sections (Left: Design I, Right: Design II)

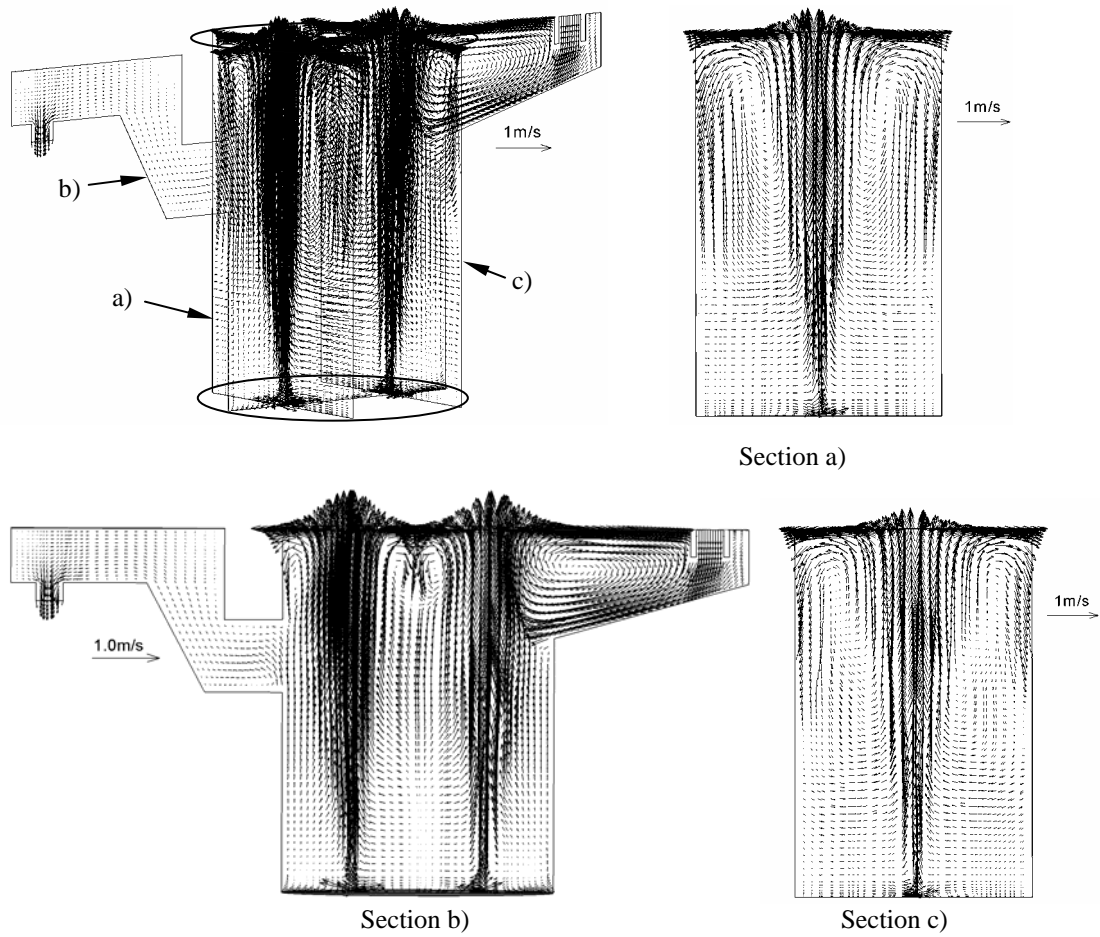


Fig.8 Velocity distributions on vertical slices in Design I

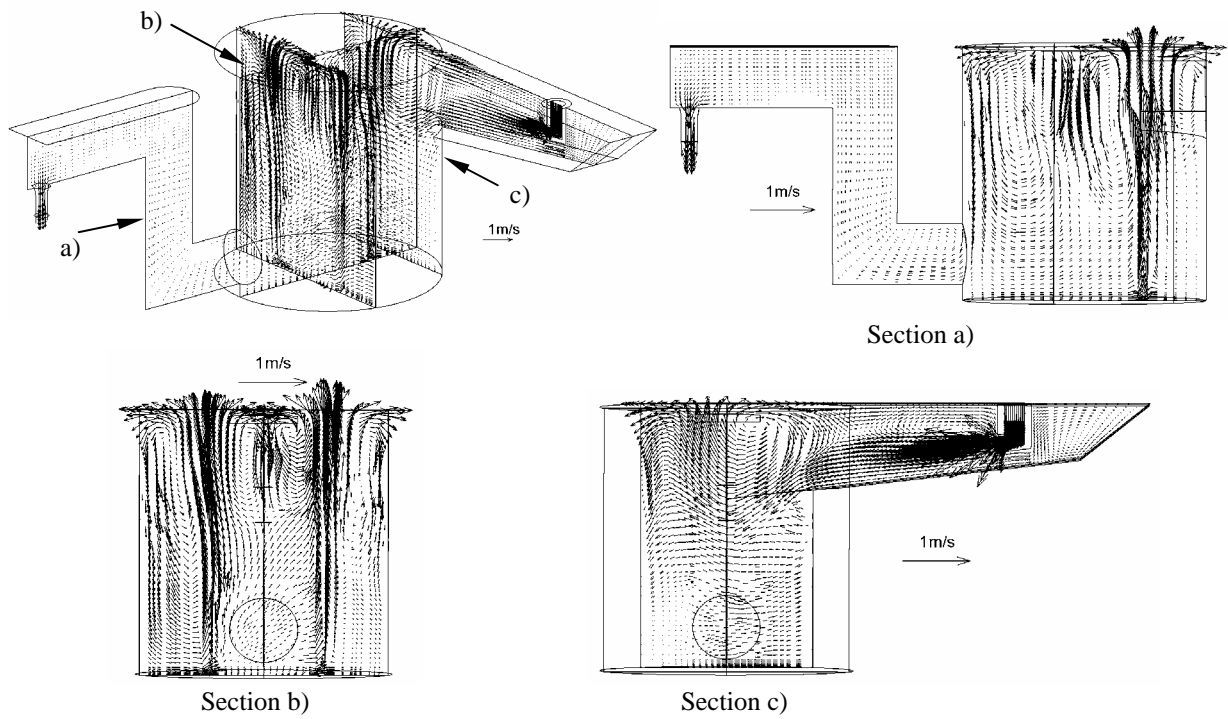


Fig.9 Velocity distributions on vertical slices in Design II

Velocity distributions on some vertical slices through the vessels are shown in **Figure 8** and **9**. The molten steel flows upwards in the gas plume and downwards along walls, generating a strong recirculation within the entire height of the vessel. Therefore particles (or



solute fluids) may recirculate a long time in the domain, as discussed later, which provides a good opportunity for chemical reactions. Fig.8 indicates again that fluid flow in Design I is stronger than in Design II. **Figure 10** shows the turbulent energy dissipation rate in the vessel. In Design I, the top surface and the gas plume have energy dissipation rates  $>1.0\text{m}^2/\text{s}^3$  (1000 W/ton), far larger than at other places. In Design II, this value is  $0.37\text{m}^2/\text{s}^3$  (370W/ton). This big stirring power at the top surface is likely to be beneficial for the chemical reactions between the molten steel and the slag.

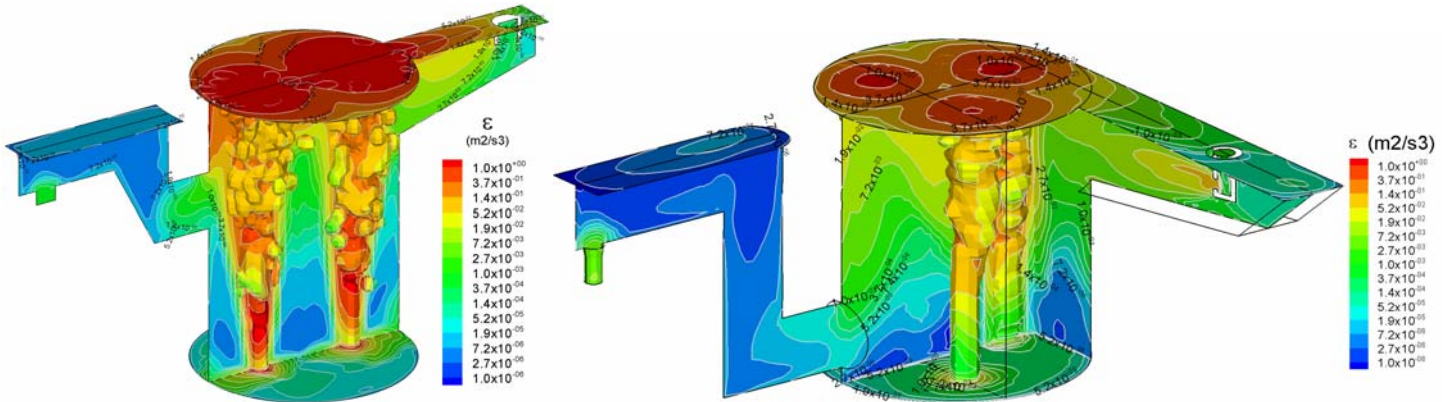


Fig.10 Turbulent energy dissipation rate in the vessel (Design I (left) and Design II (right))

### Mixing

Solute transport is calculated in order to simulate the dissolution and dispersion of the alloy added into the molten steel. Unlike the continuous nature of the real process, the solute is added here as a tracer for better visualization, and convected outflow is ignored. The place of the tracer alloy addition and points to monitor its local volume fraction change with time are shown in **Figure 11**. The alloy is added into the domain at the center plane midway between the center axis and inlet launder exit, 0.1m below the surface. **Figure 12** shows the changes of the volume fraction with time at the monitoring points. Points 8 and 9 in Design I and point 6 in Design II are close to the connection between the main vessel and the outlet launder. The earlier that alloy appears there, the more serious is the problem of short circuiting through the domain. Fig.12 and **Figure 13** indicate that the alloy starts to reach these place at only 5-7s in Design I, but is 14s in Design II. From this point of view, Design II is better than Design I. Fig.12 also indicates that the alloy volume fraction at different monitoring points fluctuates with time until converging together, and eventually dropping down with increasing time. The average volume fractions of the solute are  $2.95 \times 10^{-4}$  for Design I, and  $2.75 \times 10^{-4}$  for Design II. The time when all of the points reach the same value is defined as the mixing time. This mixing time is observed in Fig. 12 to be 90s for Design I, and 110s for Design II. From this definition, Design I has a little faster mixing than Design II. After around 2000s, all the tracer alloy has left the Oxidizer vessel to the next vessel. The theoretical residence time of the molten steel in the domain is 950s for Design I, and 1018s for Design II, which is around 10 times larger than the mixing time. Thus the mixing conditions are judged to be good in both vessels. It should be mentioned that a residence time exceeding the mixing time is sufficient for homogenization but not always enough for reactions. Of greater importance is the need to avoid short circuiting flow and to transport the inclusions to the top slag. Reactions also depend on interfacial area between the steel and gas, emulsification between steel and slag, and thermodynamics.

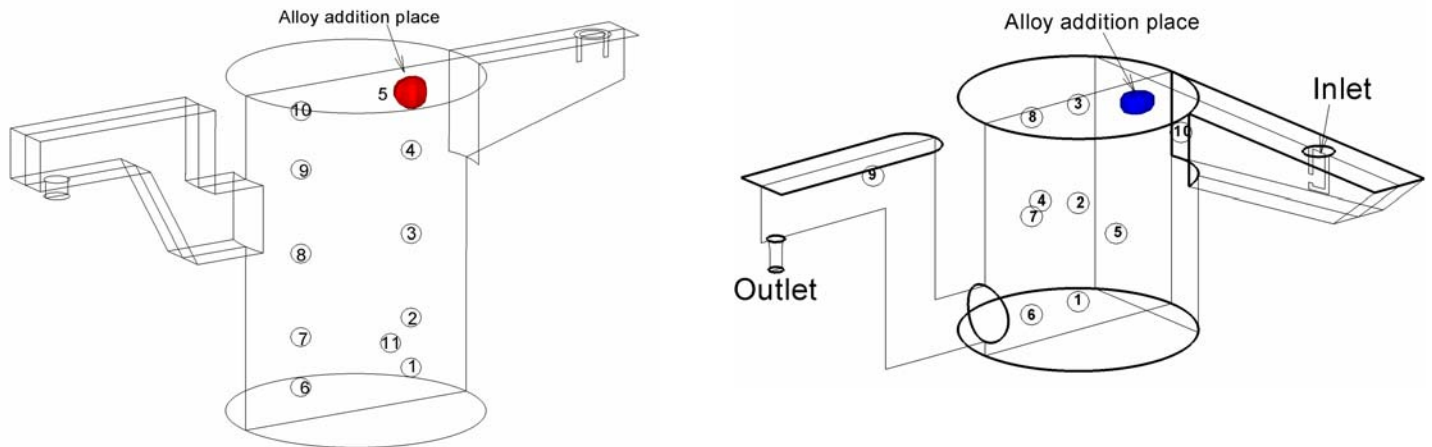


Fig.11 The addition place of the alloy and points monitoring the concentration (Left: Design I; Right: Design II)

The relationship between the mixing time and the stirring power is shown in **Figure 14**, which is consistent with the correlation of other investigations<sup>[18]</sup>. The iso-surfaces of the alloy volume concentration in the domain are shown in **Figure 15**. Design I has a flow condition similar to a pair of well-mixed vessels in series, as the two strong gas injection plumes partly separate the two flow recirculation regions in the vessel from each other. In Design II, the three gas injection jet and the swirl fluid flow avoids this behavior.

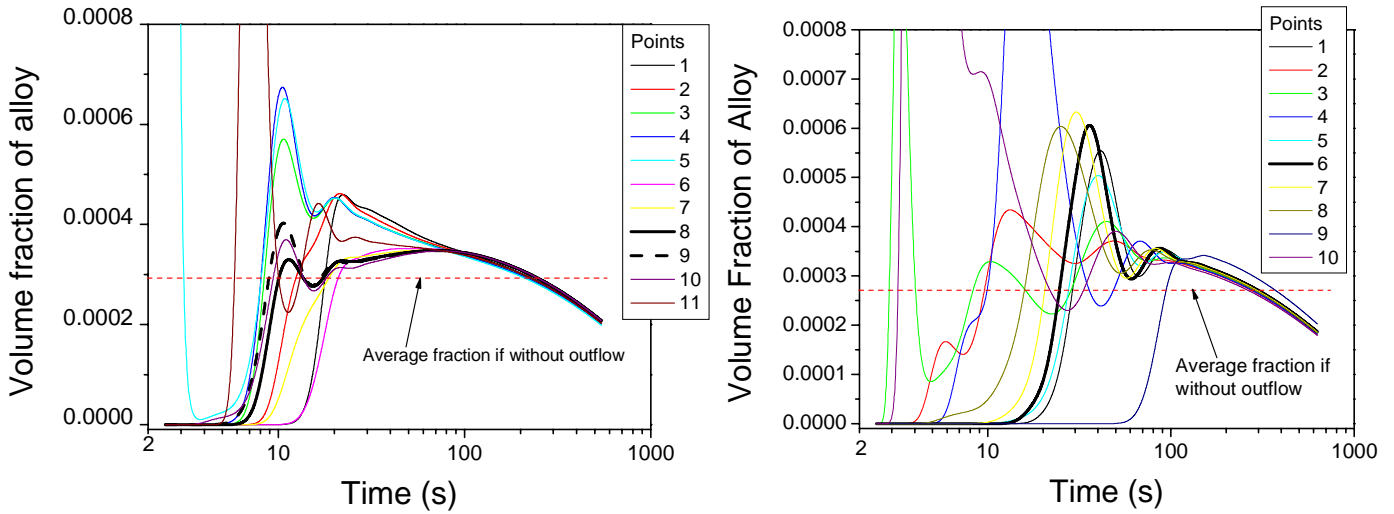


Fig.12 Dispersion of alloy in the vessel (Left: Design I; Right: Design II)

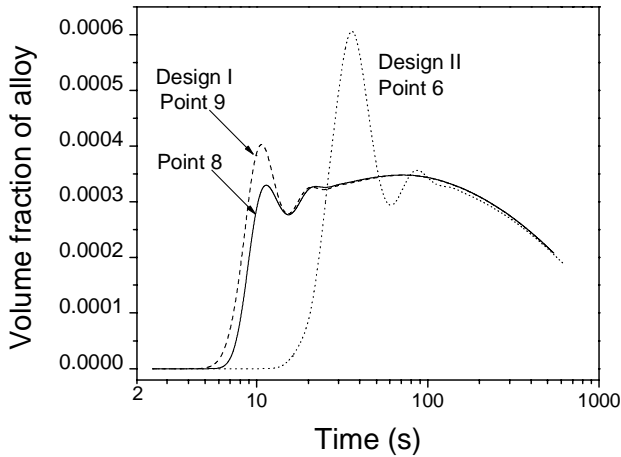


Fig.13 Alloy dispersion near the connection between the main vessel and the outlet launder

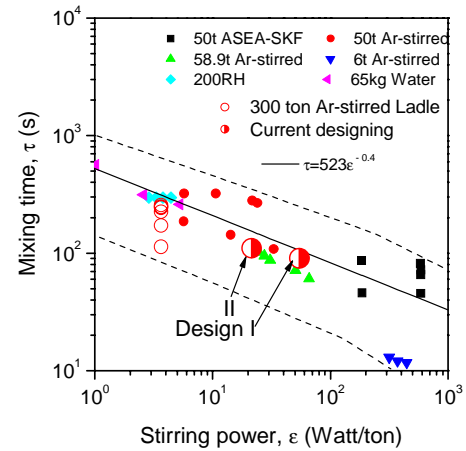


Fig.14 Mixing time as a function of stirring power of the two designs compared with literature data<sup>[18]</sup>

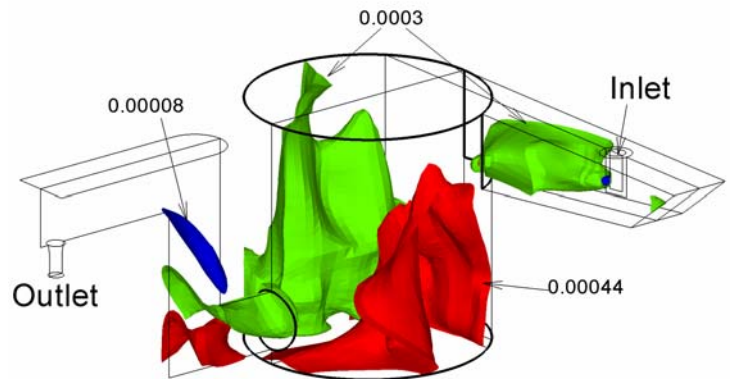
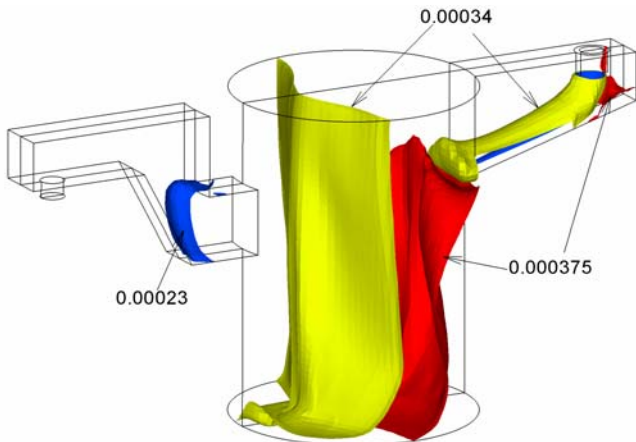
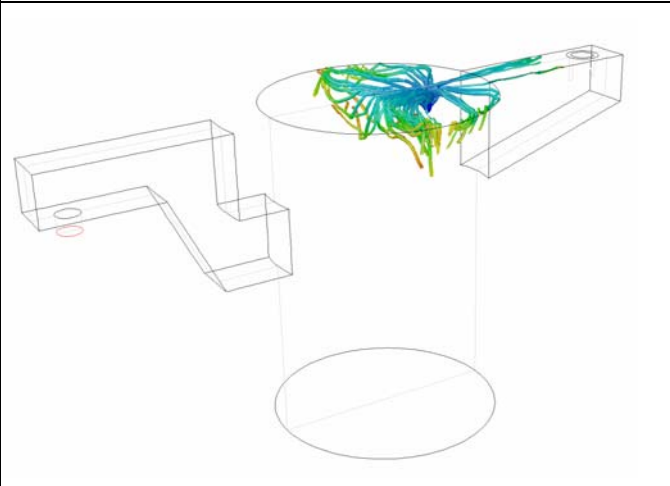
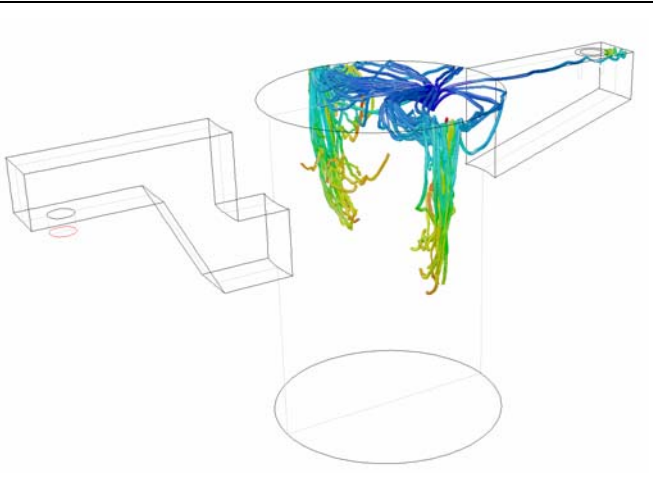
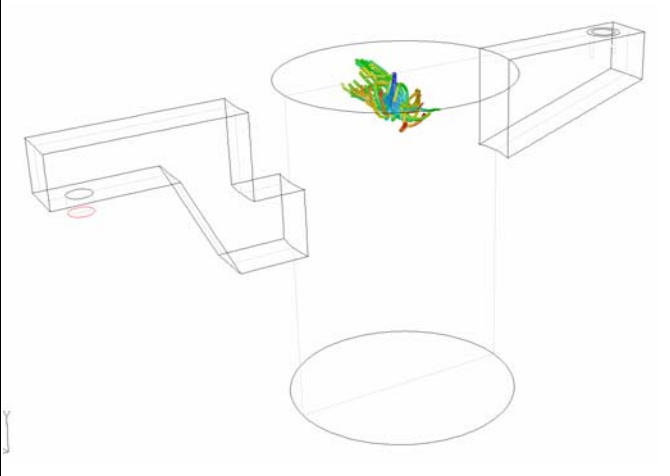
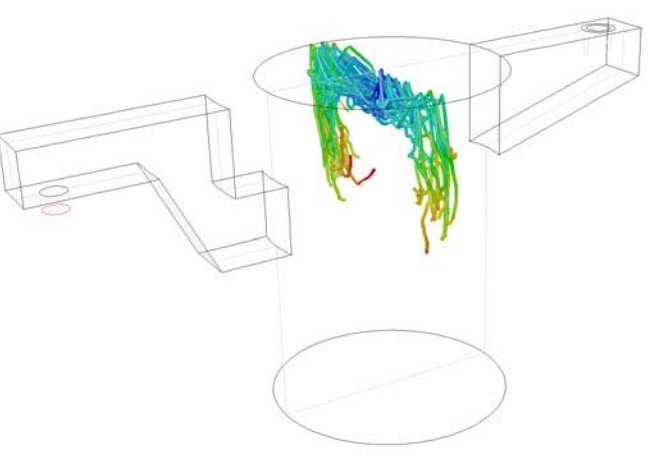


Fig.15 Alloy iso-surface at 50.5s (left: Design I; right: Design II)

Examination of the alloy addition can illustrate the mixing. Table 2 gives trajectories of 50 lumps of 100mm diameter SiMn alloy particles with density of  $6120 \text{ kg/m}^3$ . If added to the position corresponding to the eye above the first plume in Design I, as shown in Fig.11, the alloy lumps firstly disperse over the half top surface closest to the inlet launder, and a few enter the top of the inlet launder. Those above the main vessel are drawn down the vessel walls, and then accumulated to the centerplane between the two gas plumes to become entrained into the bulk of the steel, and reach around 0.5-1.0m below the top surface in 10 seconds. It was reported that this size SiMn alloy is released from its temporary steel shell in  $\sim 10\text{s}$ .<sup>[8]</sup> If the alloy is added into the domain at the top center of the main vessel, due to the downwards fluid flow there (Fig.8, section b)), the alloy lumps mainly disperse midway between the two gas plume, and downwards to the bulk. They reach 0.5-0.8m in 10 seconds. The final depth and position alloy lumps reach in the bulk are very similar between these two place alloy additions. But the non-center addition has a few lumps which first disperse over the half surface of the top and the top of the inlet launder. This difference may induce a slight difference in mixing, which will be simulated in the future.

Table 2. Effect of alloy addition place on its trajectory

	Time =3.3s	Time 10.3s
Plume-center addition (Fig.11)		
Vessel-center addition		

### Inclusion Motion in the Vessel

Figure 16 shows typical trajectories of inclusions in the vessel, which suggests that inclusions in Design I move and recirculate much longer than in Design II before removal. Table 3, 4 and Figure 17 shows the inclusion mean residence time and removal fraction. Larger inclusions naturally are removed more than smaller inclusions. The residence time of inclusions in Design I is 2.1-2.6 times larger than that in Design II. Table 3 indicates that Design II removed more inclusions than Design I. For  $50\mu\text{m}$  inclusions Design I can remove 88.5%, Design II removes 96.5%. Design I removes 91%  $100\mu\text{m}$  inclusions, while Design II removes 97.5%.  $300\mu\text{m}$  are all removed with both Design I and Design II. In Design II, large inclusions such as  $300\mu\text{m}$  inclusions are more removed to the top of the inlet launder than Design I. Inclusions reaching the top of the outlet launder in Design II is less than 2% for each size, which is less than that of Design I. The results indicate that although the mixing in Design I is a little faster than Design II, Design II appears to be more efficient for inclusion removal.

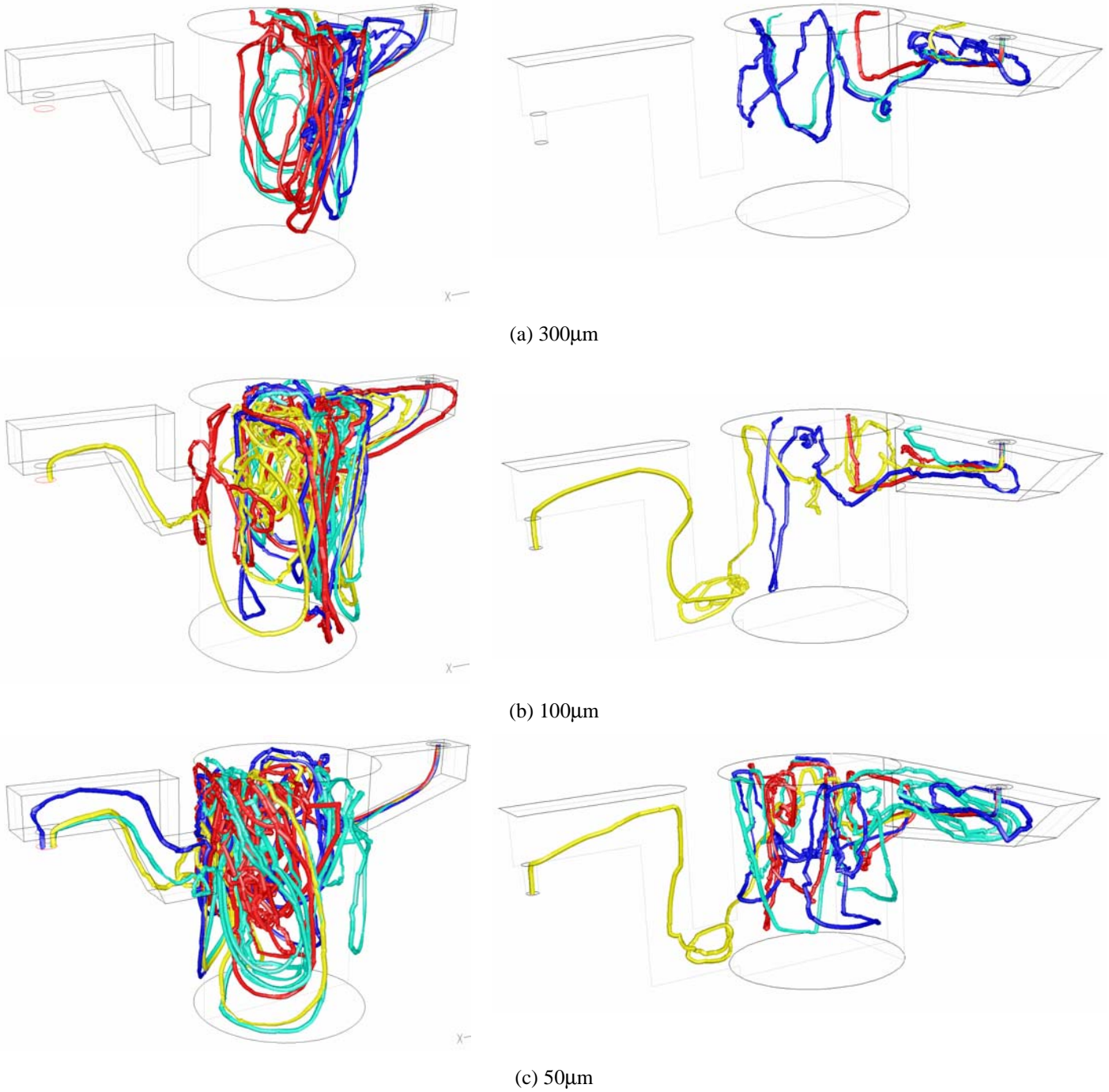


Fig.16 Typical trajectories of 4 inclusion particles each in Design I (left) and Design II (right)

Table 3 Mean residence time of inclusions

	Inclusion size	Design I					Design II				
		Top of inlet launder	Top of outlet launder	Top of cylindrical section	Outlet	Mean	Top of inlet launder	Top of outlet launder	Top of cylindrical section	Outlet	Mean
Mean residence time (s)	50µm	85.7	269.7	109.6	226.7	<b>121.6</b>	25.7	144.3	47.0	181.7	<b>49.8</b>
	100µm	65.2	215.2	96.9	205.4	<b>100.3</b>	24.92	146.9	44.4	201.6	<b>46.8</b>
	300µm	42.7	171.2	70.4	221.0	<b>70.2</b>	13.71	262.8	35.5	-	<b>27.2</b>



Table 4 Inclusion removal fraction

	Inclusion size	Design I					Design II				
		Top of inlet launder	Top of outlet launder	Top of cylindrical section	Outlet	Total Removal	Top of inlet launder	Top of outlet launder	Top of cylindrical section	Outlet	Total Removal
Removal fraction (%)	50 $\mu\text{m}$	14.3	1.3	72.9	11.5	<b>88.5</b>	12.6	0.7	83.2	3.5	<b>96.5</b>
	100 $\mu\text{m}$	15.4	2.7	72.9	9.0	<b>91.0</b>	15.9	1.5	80.1	2.5	<b>97.5</b>
	300 $\mu\text{m}$	19.7	5.1	75.2	0.1	<b>99.9</b>	49.5	1.1	49.4	-	<b>100</b>

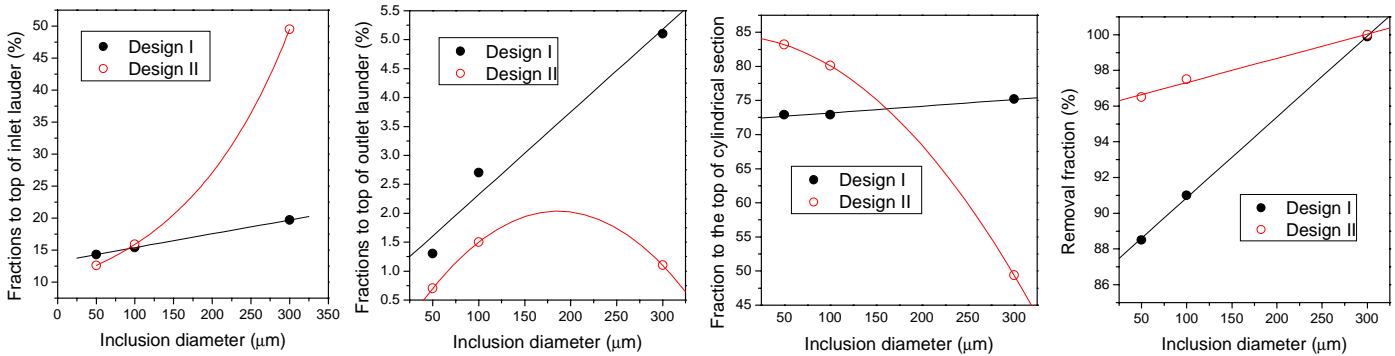


Fig.17 Fractions of inclusions to different destinations

The calculated residence time of solute particles, theoretical residence time, residence time of inclusions and bubbles, and mixing time are summarized in **Table 5**. The residence time of bubbles in the vessel is 0.87-1.24s, which is governed mainly by the vessel height, and is far smaller than the residence times of solute, inclusions and steel. Thus inclusions may be removed faster by attaching to the surface of the bubbles. However, the attachment probabilities between inclusions and  $>30\text{mm}$  bubbles are very small.<sup>[19]</sup> The current gas injection rate through 3 plugs (Design II) produces smaller bubbles (31.0mm) than through 2 plugs (Design I, 36.4mm). It was reported that small bubbles also improve the mixing in the molten steel during ladle gas bubbling process<sup>[12]</sup>. Thus, smaller bubbles might improve inclusion removal and mixing, favoring Design II over Design I for the current continuous steelmaking process.

Table 5 Residence time and mixing time (s)

	Theoretical residence time	Residence time of $>50\mu\text{m}$ inclusions ( $5000\text{kg/m}^3$ )	Residence time of bubbles ( $1.6228\text{ kg/m}^3$ )	Mixing time
Design I	950	70.2-121.6	1.24	90s
Design II	1018	27.2-49.8	0.87	110s

## SUMMARY

Advanced computational fluid dynamics (CFD) models of turbulent, multiphase flow are applied to design a new scrap-based process for continuous steelmaking. The current work focuses on comparing transient fluid flow, alloy mixing, and inclusion particle transport in two different designs of the Oxidizer vessel. This vessel is cylindrical, with an inlet launder and an outlet launder. The models are three-dimensional and use the Eulerian-Lagrangian method for multiphase flow, the  $k-\epsilon$  model for turbulence, species diffusion equation for alloy mixing, the random walk Lagrangian method for particle transport, and are based on FLUENT. The effect of the arrangement of inlet and outlet launders on the fluid flow, residence time, mixing time, inclusion removal fractions are investigated. The design with a side opened inlet nozzle diminishes jet impingement on the bottom of the inlet launder. The design with inlet launder not in the same line as the outlet launder produces swirl, which stabilizes the flow pattern, avoids short circuiting, and likely lessens variability in the product. This swirl design has more inclusion removal and roughly the same mixing conditions as the design without swirl.

The current work represents an important but very rough preliminary step towards designing a new metallurgical process. Fluid flow and mixing have been modeled, but of greater importance is the control of interfacial chemical reactions and variability. This work is a necessary first step towards performing calculations of these relevant practical phenomena. Future model investigations will include:

- Consideration of multi-size bubbles, other inter-phase forces etc;
- Inclusion nucleation, growth, and collision with each other and with gas bubbles;
- Top surface waves, and interfacial phenomena such between gas and steel, and between steel and slag (slag emulsification);
- Chemical reactions between top slag and the molten steel such as De-P and De-S and the reaction De-C, coupled with fluid flow;
- Heat transfer phenomena during this continuous steelmaking process;
- Design of other vessels by numerical simulation and parametric studies.

## ACKNOWLEDGEMENT

This material is based upon work supported by the U.S. Department of Energy under cooperative agreement number DE-FC36-03ID14279. Such support does not constitute an endorsement by DOE of the views expressed in the article. The authors also appreciate the support of the Continuous Casting Consortium at UIUC and the National Science Foundation (Grant # 0115486).

## REFERENCES

- [1]. J. Peter, K.D. Peaslee and D.G.C. Robertson, "Study of Current Steelmaking Practices to Evaluate the Viability of Continuous Steelmaking," in AISTech 2004 Iron & Steel Conference Proceedings, Vol. 1, AIST, Warrandale, PA, (Nashville TN, September 2004), 2004, 1071-1083.
- [2]. J.-P. Birat, "Innovation Paradigms for the Steel Industry of the 21st Century Future Direction for Steel Industry and Continuous Casting," in Innovation and Excellence in Continuous Casting-Dedicated to Dr. Manfred Michael Wolf, H. Marti, ed. Stahl Eisen, 2003, 129-161.
- [3]. J. Peter, K.D. Peaslee and D.G.C. Robertson, "Introduction of a novel, scrap-based, fully continuous steelmaking process," in AISTech 2005 Iron & Steel Conference Proceedings, AIST, Warrandale, PA, (Charlotte NC, USA, May 9-12, 2005), 2005, in press.
- [4]. L. Zhang and B.G. Thomas, "Report on DOE Project: Development of a Process to Continuously Melt, Refine, and Cast High-Quality Steel---Fluid Flow, Mixing and Inclusion Motion in Bottom Gas-Stirred Molten Steel Vessel," Report, University of Illinois at Urbana-Champaign, 2003.
- [5]. L. Zhang and B.G. Thomas, "Report on DOE Project: Development of a Process to Continuously Melt, Refine, and Cast High-Quality Steel---Transient Model of Transport of Molten Steel and Inclusions in a Bottom Gas-Stirred Vessel," Report, University of Illinois at Urbana-Champaign, 2003.
- [6]. J. Peter, "Personal Communication: Fluid Flow and Mixing Phenomena in a Water Model Cone Shape Vessel", personal communication, 2004.
- [7]. J. Aoki, B.G. Thomas, J. Peter, K.D. Peaslee, "Experimental and Theoretical Investigation of Mixing in a Bottom Gas-Stirred Ladle," in AISTech2004, ISS, Warrandale, PA, 2004, 1045-1056.
- [8]. J. Aoki, L. Zhang and B.G. Thomas, "Modeling of inclusion removal in ladle refining," in ICS 2005 - The 3rd International Congress on the Science and Technology of Steelmaking, AIST, Warrandale, PA, (May 9-12, 2005, Charlotte, NC), 2005, In press.
- [9]. B.G. Thomas, Q. Yuan, S. Sivaramakrishnan, T. Shi, S.P. Vanka, M.B. Assar, "Comparison of Four Methods to Evaluate Fluid Velocities in a Continuous Casting Mold," ISIJ Int., Vol. 41 (10), 2001, 1262-1272.
- [10]. B.E. Launder and D.B. Spalding, "Numerical Computation of Turbulent Flows," Comp. Meth. Applied Mechanics and Engr., Vol. 13 (3), 1974, 269-289.
- [11]. A. Haider and O. Levenspiel, "Drag Coefficient and Terminal Velocity of Spherical and Nonspherical Particles," Powder Technology, Vol. 58, 1989, 63-70.
- [12]. L. Zhang, "Mathematical Simulation of Fluid Flow in Gas-Stirred Liquid Systems," Modelling Simul. Mater. Sci. Eng., Vol. 8 (4), 2000, 463-476.
- [13]. L. Zhang and B.G. Thomas, "Fluid Flow and Inclusion Motion in the Continuous Casting Strand," in Steelmaking National Symposium Mexico, (Morelia, Mich, Mexico), 2003.
- [14]. B.G. Thomas and F.M. Najjar, "Finite-Element Modeling of Turbulent Fluid Flow and Heat Transfer in Continuous Casting," Applied Mathematical Modeling, Vol. 15 (5), 1991, 226-243.
- [15]. D.E. Hershey, B.G. Thomas and F.M. Najjar, "Turbulent Flow through Bifurcated Nozzles," Int. J. Num. Meth. in Fluids, Vol. 17 (1), 1993, 23-47.
- [16]. FLUENT6.1-Mannual, Report, Fluent Inc., Lebanon, New Hampshire, 2003.
- [17]. S.T. Johansen, D.G.C. Robertson, K. Woje, T.A. Engh, "Fluid Dynamics in Bubble Stirred Ladles: Part I. Experiments," Metall. Trans., Vol. 19B, 1988, 745-754.
- [18]. L. Zhang, B.G. Thomas, K. Cai, L. Zhu, J. Cui, "Inclusion Investigation during Clean Steel Production at Baosteel," in ISSTech2003, ISS, Warrandale, PA, 2003, 141-156.
- [19]. L. Zhang, J. Aoki and B.G. Thomas, "Inclusion Removal by Bubble Flotation in Continuous Casting," in Materials Science & Technology 2004 (MS&T'04), Vol. 2, TMS & AIST, Warrandale, PA, (Sep.26-29, 2004, New Orleans, Louisiana, USA), 2004, 161-178.